

Cross Validation of TEMPEST-D and RainCube Observations Over Precipitation Systems

Chandrasekar Radhakrishnan , V. Chandrasekar, *Fellow, IEEE*, Steven C. Reising , *Senior Member, IEEE*, Wesley Berg , Shannon T. Brown , *Senior Member, IEEE*, Simone Tanelli , Ousmane O. Sy , and Gian Franco Sacco

Abstract—This article presents cross validation of nearly simultaneous observations between the Temporal Experiment for Storms and Tropical Systems-Demonstration (TEMPEST-D) and Radar in a CubeSat (RainCube) satellite microwave sensors over precipitation systems. RainCube senses the atmosphere using a *K*-band nadir-pointing radar, and TEMPEST-D senses using multifrequency millimeter-wave radiometers. Nine precipitation systems were used in this cross-validation study. Occurring over nearly a two-year period, these storms were scattered over many regions of the world from the Tropics to the midlatitudes. A shift correction algorithm was developed to remove the uncertainty between the two sensors' observations due to the time difference and the storm motion between the two instrument overpasses. Correlation coefficients were calculated between self-normalized, inverted RainCube cumulative reflectivity and self-normalized TEMPEST-D brightness' temperatures. As expected, these correlation coefficients are consistently higher for the four TEMPEST-D high-frequency channels than for the single low-frequency channel. The shift correction algorithm improved the average correlation coefficient by 19% for the four high-frequency channels and by 58% for the single low-frequency channel. The average correlation coefficient after shift correction is 0.76 for TEMPEST-Ds four high-frequency channels and 0.54 for the single low-frequency channel. The comparisons demonstrated high consistency between the TEMPEST-D and RainCube observations, even though the two microwave sensors' fundamental physics is different; one is passive, and the other is active.

Index Terms—CubeSats, radar in a CubeSat (RainCube), smallsats, temporal experiment for storms and tropical systems-demonstration (TEMPEST-D).

Manuscript received 14 April 2022; revised 1 June 2022 and 14 July 2022; accepted 2 August 2022. Date of publication 17 August 2022; date of current version 20 September 2022. This work was supported in part by the NASA Earth Venture Technology Demonstration Program under Grant NNX15AP56G, Grant 80NSSC20K1124, and Grant 80NSSC21K2073 to Colorado State University and in part by NASA's Earth Science Division ESTO, Flight and R&A Programs. (Corresponding author: Chandrasekar Radhakrishnan.)

Chandrasekar Radhakrishnan is with the Cooperative Institute for Research in the Atmosphere, Colorado State University, Fort Collins, CO 80523 USA (e-mail: chandrasekar.radhakrishnan@colostate.edu).

V. Chandrasekar and Steven C. Reising are with the Department of Electrical and Computer Engineering, Colorado State University, Fort Collins, CO 80523 USA (e-mail: chandra@colostate.edu; steven.reising@colostate.edu).

Wesley Berg is with the Department of Atmospheric Science, Colorado State University, Fort Collins, CO 80523 USA (e-mail: wesley.berg@colostate.edu).

Shannon T. Brown, Simone Tanelli, and Ousmane O. Sy are with the Jet Propulsion Laboratory (JPL), California Institute of Technology, Pasadena, CA 91109 USA (e-mail: shannon.t.brown@jpl.nasa.gov; simone.tanelli@jpl.nasa.gov; ousmane.o.sy@jpl.nasa.gov).

Gian Franco Sacco is with the Praesidium Inc., St. George, UT 84790 USA (e-mail: gianfranco.sacco@jpl.nasa.gov).

Digital Object Identifier 10.1109/JSTARS.2022.3199402

I. INTRODUCTION

UNDERSTANDING cloud microphysics is essential for studying the formation and evolution of precipitation systems. The time scale of most cloud microphysics processes is short, and high temporal resolution measurements are needed to properly capture them. Ground weather radar networks can observe the atmosphere with very high temporal resolution [1]. Many studies [2], [3], [4] have used weather radar observations to analyze the evolution of cloud microphysical processes within storms. However, ground weather radars provide observations over land, and a few observations are available near coastal regions, but no ground weather radars provide coverage over the open ocean. The prediction skills of numerical weather and climate models mainly depend on the model's initial conditions [5], [6], [7] and physics parameterization schemes [8], [9], [10]. Open ocean observations are essential to generate acceptable initial conditions for numerical weather prediction (NWP) models, especially to predict severe weather events, such as hurricanes, typhoons, and tropical cyclones. In addition, open ocean measurements are required to validate and improve NWP models' physics parameterization schemes over the ocean. Open ocean observations are also crucial to analyze the variability of precipitation over the oceans. Knowledge of these variations is needed to study and predict climate change and inform environmental policies.

Weather satellite observations play an increasingly crucial role in providing critical oceanic observations on a global basis. Depending on the applications and requirements, weather satellites are deployed either in geosynchronous equatorial orbit (GEO) or low Earth orbit (LEO). Presently, weather sensors on GEO satellites provide observations only in the visible and infrared (IR) wavelength ranges. Visible and IR sensors measure only the locations of clouds and cloud top temperatures. They cannot penetrate the cloud to observe the cloud microphysics and surface precipitation. Sensors on LEO satellites also include microwave radiometers, either with or without IR and visible sensors. Microwave radiometers can penetrate the cloud to measure cloud microphysics and surface precipitation characteristics. However, the main limitation of LEO satellites is their low temporal resolution due to long revisit times. Therefore, it is challenging to study the growth and decay of individual storms using LEO satellites. A constellation of satellites could overcome these limitations by deploying identical sensors

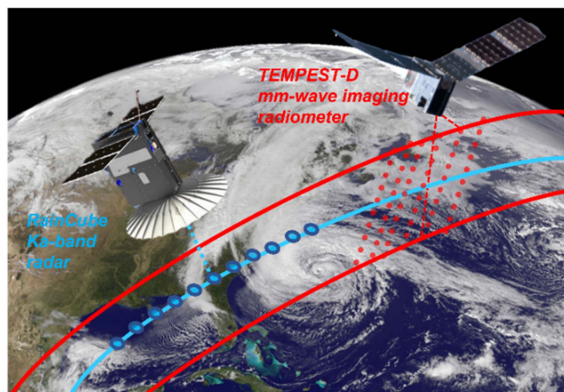


Fig. 1. Illustration of RainCube (in blue) and TEMPEST-D (in red) overpasses, where the two CubeSats are orbiting in the same direction. The RainCube satellite is shown on the left, and the TEMPEST-D CubeSat is shown on the right.

with much more frequent revisit times [11]. However, when using traditional satellite technology, producing and deploying a satellite constellation is very expensive. Nevertheless, CubeSat technology has been recently demonstrated as a viable low-cost option. As of March 2022, more than 1594 CubeSats had been launched [12]. Since CubeSats' fabrication and launch costs are relatively low, including both spacecraft and instruments, it is possible to deploy a constellation of CubeSats in LEO to enable improved temporal resolution of global observations. However, before using CubeSat observations for operational product generation, merging their data with other traditional satellite observations or assimilating them into NWP models, it needs to be validated with equivalent traditional satellite observations and corresponding ground-based observations. Studies have assessed the performance of CubeSats using other observations. Berg et al. [13] conducted a calibration and validation study of Temporal Experiment for Storms and Tropical Systems – Demonstration (TEMPEST-D) observations with multiple well-calibrated sensors, including the Global Precipitation Measurement (GPM) Microwave Imager (GMI) as well as four Microwave Humidity Sounder (MHS) sensors aboard National Oceanic and Atmospheric Administration and European Space Agency/EUMETSAT MetOp satellites. Their analysis demonstrated that the absolute calibration accuracy of TEMPEST-D is within 1 K and calibration precision, or stability over time, is within 0.6 K for all five channels. Christophersen et al. [14] successfully assimilated the simulated radiances expected from future Time-Resolved Observations of Precipitation structure and storm Intensity with a Constellation of Smallsats (TROPICS) CubeSats and showed potential improvements in tropical cyclone prediction.

Radhakrishnan et al. [15] cross-validated TEMPEST-D and GPM GMI brightness temperature (TB) observations over precipitation systems and concluded that the two sets of observations have good agreement. Their analysis also showed that when TEMPEST-D observations are combined with those from GMI, this can double the number of observations and improve the temporal frequency of measurements over severe weather events.

Schulte et al. [16] retrieved atmospheric water vapor, cloud liquid water path, and cloud ice water path from TEMPEST-D TB observations. They showed that the retrieved products match well with the same products retrieved from similar but more expensive and larger MHS sensors' observations. Radhakrishnan et al. [17] used TEMPEST-D TB observations to successfully estimate surface rainfall. These studies showed that CubeSats could measure the atmosphere as well as traditional satellites. To continue the validation of CubeSat observations, this study cross-validated observations from two CubeSats, TEMPEST-D and radar in a CubeSat (RainCube).

The rest of this article is organized as follows. Section II describes the TEMPEST-D and RainCube missions. Section III discusses the methodology followed to compare the two observations. In Section IV, the data are presented, while in Section V, the results are presented. Finally, Section VI concludes this article.

II. TEMPEST-D AND RAINCUBE SATELLITE MISSIONS

Temporal Experiment for Storms and Tropical Systems (TEMPEST) is a 6U CubeSat mission concept to observe the evolution of cloud convective systems with high temporal resolution. The concept of TEMPEST constellation mission is to deploy six to eight identical 6U CubeSats in the same orbital plane with approximately 5-min spacing [18]. TEMPEST-D (“D” for demonstration) satellite is a single 6U CubeSat launched on May 21, 2018 and deployed into orbit on July 13, 2018. The TEMPEST-D radiometers measure at five millimeter-wave frequencies (87, 164, 174, 178, and 181 GHz) that provide detailed information on convection as well as the surrounding water vapor environment. The TEMPEST-D spatial resolution at nadir is 25 km for 87 GHz and 12.5 km at 181 GHz from a nominal orbital altitude of 400 km. A detailed description of the instrument and prelaunch calibrations are provided in [19]. Calibration and validation of the TEMPEST-D instrument have demonstrated equivalent performance to the traditional satellites, as discussed in [13]. RainCube is the first-ever radar instrument in a 6U CubeSat. It is a joint development between the Jet Propulsion Laboratory and Tyvak NanoSatellite Systems (Tyvak). RainCube has a 35.75 GHz (*Ka*-band) nadir-pointing precipitation profiling radar payload deployed from the ISS on July 13, 2018. The peak transmit power of RainCube's radar is 10 W, and it has a sensitivity of 13 dBZ. The horizontal resolution of RainCube radar at the surface is 7.9 km, and the vertical resolution is 120 m. The design and technical details of RainCube are described in [20] and the products are discussed in [21]. Fig. 1 shows a graphical view of RainCube (in blue) and TEMPEST-D (in red) overpasses. The National Aeronautics and Space Administration supported these two CubeSat missions for on-orbit validation of technology for studying the Earth's atmosphere.

III. METHODOLOGY

Cross comparison of TEMPEST-D and RainCube observations consists of two parts. The first part is to identify nearly simultaneous overpasses over precipitating systems by RainCube

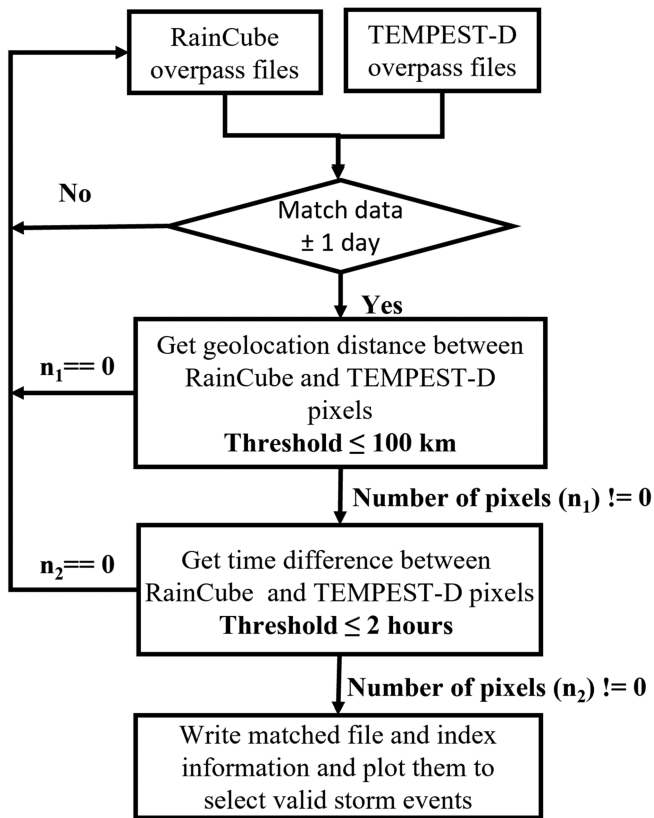


Fig. 2. Automated algorithm to identify nearly simultaneous overpasses between RainCube and TEMPEST-D over precipitating systems.

and TEMPEST-D. The second part is to determine parameters from two observations that are meaningful to compare and develop an algorithm to correct the shift between the two observations to maximize the correlation. In the first part, an automated algorithm has been developed to identify nearly simultaneous overpasses. The algorithm consists of the following four steps, as shown in detail in Fig. 2.

- 1) The first step is to read the RainCube overpass date and find the closest date of a TEMPEST-D overpass. If a TEMPEST-D overpass is available within \pm one day of the RainCube overpass, then the algorithm proceeds to the second step. If not, the algorithm continues to the next RainCube overpass.
- 2) The second step is to determine the number of pixels (n_1) in which a geolocated distance between the two datasets is less than 100 km. If n_1 is not equal to zero, the algorithm proceeds to the third step. If none of the pixel distances are less than 100 km, the algorithm continues to the next RainCube overpass.
- 3) The third step is to calculate the time difference between two observations to determine the number of pixels (n_2), which have a time difference of less than 2 h. If n_2 is not equal to zero, the algorithm will proceed to the fourth step. If n_2 is equal to zero, the algorithm continues to the next RainCube overpass.

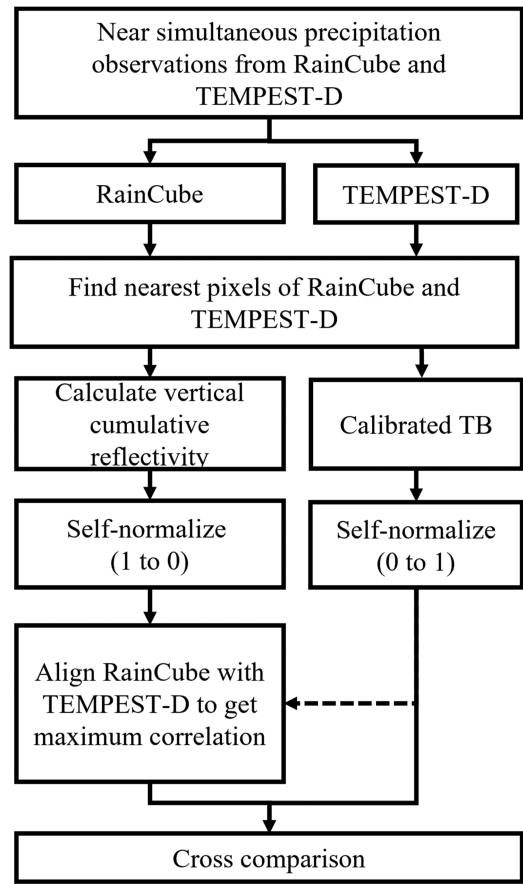


Fig. 3. Procedure followed to cross-validate RainCube and TEMPEST-D observations over precipitation systems.

- 4) The fourth step is to store the detailed data for both the RainCube and TEMPEST-D overpasses and plot them to select precipitation events observed by both RainCube and TEMPEST-D.

The second part of cross validation is to use the nearly simultaneous overpasses identified in the first part and performs cross comparisons. Fig. 3 shows the procedure followed for the cross-comparison process. The process consists of the following five steps to compare nearly simultaneous TEMPEST-D and RainCube observations.

- 1) The first step is to find the TEMPEST-D pixels nearest to RainCube pixels for collocation.
- 2) The second step is to develop parameters from RainCube and TEMPEST-D observations for cross comparison. The TEMPEST-D TB observations are each the result of a radiative transfer integral over the entire column of the storm. To obtain an analogous observation from RainCube, the nadir reflectivity observations from all layers are vertically integrated to obtain the cumulative reflectivity (Ref_{cum}). The estimated Ref_{cum} is used for analysis along with TEMPEST-D TBs.
- 3) Since the RainCube Ref_{cum} and TEMPEST-D TB observations are on different scales and have different units, in

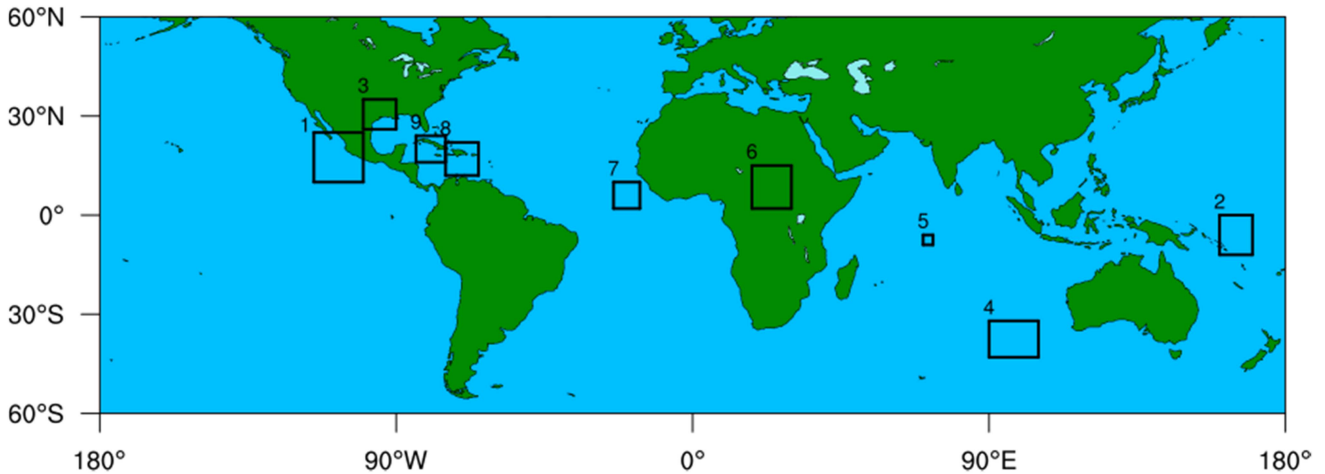


Fig. 4. Selected storm events and regions on a global map. The boxes indicate the regions considered for nearly simultaneous TEMPEST-D and RainCube overpasses over precipitation systems.

the third step, each of these observations is self-normalized between 0 and 1. The TEMPEST-D TBs represent upwelling microwave radiation and decrease due to interaction with atmospheric liquid and frozen hydrometeors, cloud liquid water, water vapor, and oxygen. On the other hand, the reflectivity factor of RainCube increases due to the backscatter of microwave radiation [22]. To account for this physical difference between sensing modalities and to obtain a clear visualization for determining the cross correlation, the RainCube self-normalized values are “inverted,” i.e., subtracted from unity. These self-normalized and inverted RainCube observations are used in further joint analysis with the self-normalized TEMPEST-D observations.

- 4) The fourth step is to perform a shift correction between the two observations. This shift correction eliminates the uncertainty due to the time difference between two observations and storm motion between the TEMPEST-D and RainCube observations. The shift correction algorithm optimally shifts the RainCube observations to match the location of lowest inverted self-normalized RainCube, Ref_{cum} , to the lowest self-normalized TEMPEST-D TB location. The amount of shift correction is chosen to maximize the correlation between the inverted RainCube cumulative reflectivity and the TEMPEST-D TBs. The shift correction algorithm is performed separately for each case since the required shift correction depends on the time difference between TEMPEST-D and RainCube observations as well as the dynamics of the precipitation system.
- 5) The final step is to perform a cross comparison between collocated and shift corrected observations.

IV. DATA USED

The analysis presented here used publicly available TEMPEST-D Level 1b data (<https://tempest.colostate.edu/data/>), containing calibrated, geolocated TBs, as well as Earth viewing angles, for all five TEMPEST-D channels. In addition,

the publicly available RainCube data (<https://tcis.jpl.nasa.gov/data/raincube/>) used here are calibrated, geolocated reflectivities as a function of altitude, as well as ground elevation data derived from digital elevation maps. All available observations from TEMPEST-D and RainCube are used in the study. Nine valid precipitation events were identified using the algorithm as nearly simultaneous overpasses. Fig. 4 shows the locations of the selected events on a global map, and Table I lists the event dates and regions of the world. The boxes, as shown in Fig. 4, indicate the regions considered for TEMPEST-D and RainCube overpasses over precipitation systems. These geographic areas are chosen to visualize the TEMPEST-D TBs at 164 GHz as well as the corresponding RainCube orbits, as shown in Figs. 5, 7, 9, and 11. Only the pixels common to TEMPEST-D and RainCube data were used for cross validation between the two sensors. The storm observations for the events numbered 1, 2, 6, and 9, as highlighted in bold in Table I, are shown in detail in Fig. 5, Fig. 7, Fig. 9, and Fig. 11, respectively. However, all nine events are used in the quantitative cross comparisons, as listed in Tables II–IV.

V. RESULTS AND DISCUSSION

Nine cases over diverse regions of the world during nearly a two-year period were identified for cross comparison of TEMPEST-D and RainCube over precipitating systems. For these cases, validation analysis is performed, and results are reported for all five TEMPEST-D channels. For brevity, the TB maps and time series results using only the 164 GHz channel are provided here.

A. Storm Over Mexico’s Pacific Coast

Fig. 5(a) shows the TEMPEST-D 164 GHz TB observations of the storm over Mexico’s Pacific coast on October 15, 2018 along with the RainCube orbit. Fig. 5(b) shows the RainCube observed vertical reflectivity profile for the same storm. The time difference between the two observations was less than 12 min. For this storm case, both CubeSats were orbiting along nearly

TABLE I
SELECTED STORM EVENT DATES AND REGIONS

Event number	Date	Region
1	October 15, 2018	Storm over Mexico's Pacific coast
2	October 15, 2018	Storm over South Pacific Ocean near the Solomon Islands
3	January 23, 2019	Storm near Houston, Texas
4	April 29, 2019	Storm over Southern Indian Ocean
5	July 21, 2019	Storm over Arabian Sea
6	June 24, 2020	Storm over Central African Republic
7	June 28, 2020	Storm over North Atlantic Ocean
8	August 23, 2020	Hurricane Laura in the Caribbean
9	August 24, 2020	Hurricane Laura in the Caribbean

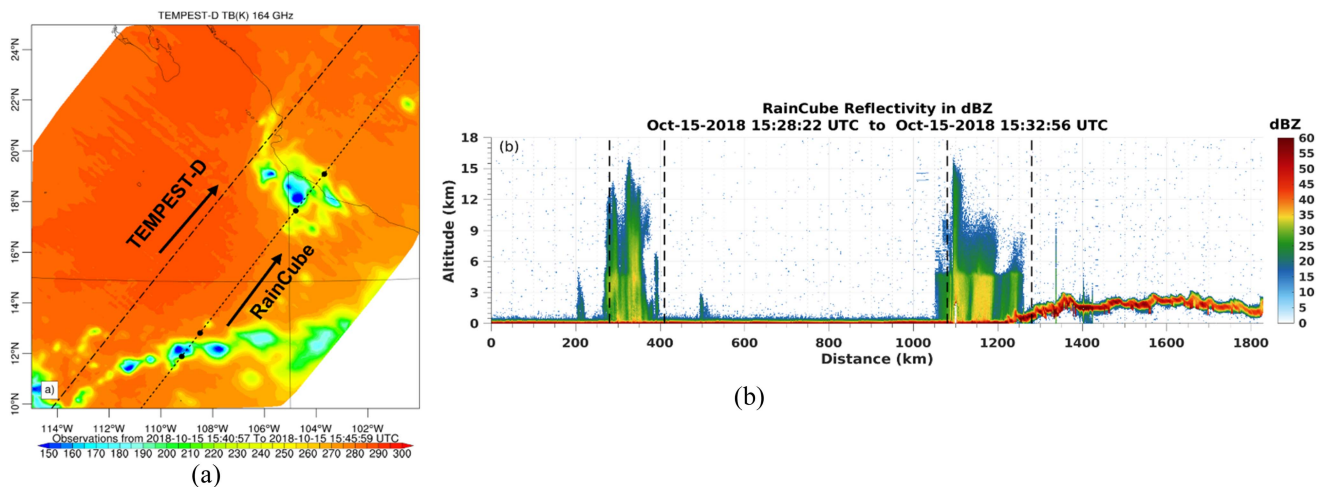


Fig. 5. (a) TEMPEST-D observed storm over Mexico's Pacific coast on October 15, 2018 and the corresponding RainCube orbit. (b) RainCube vertical reflectivity profile observations from the same storm.

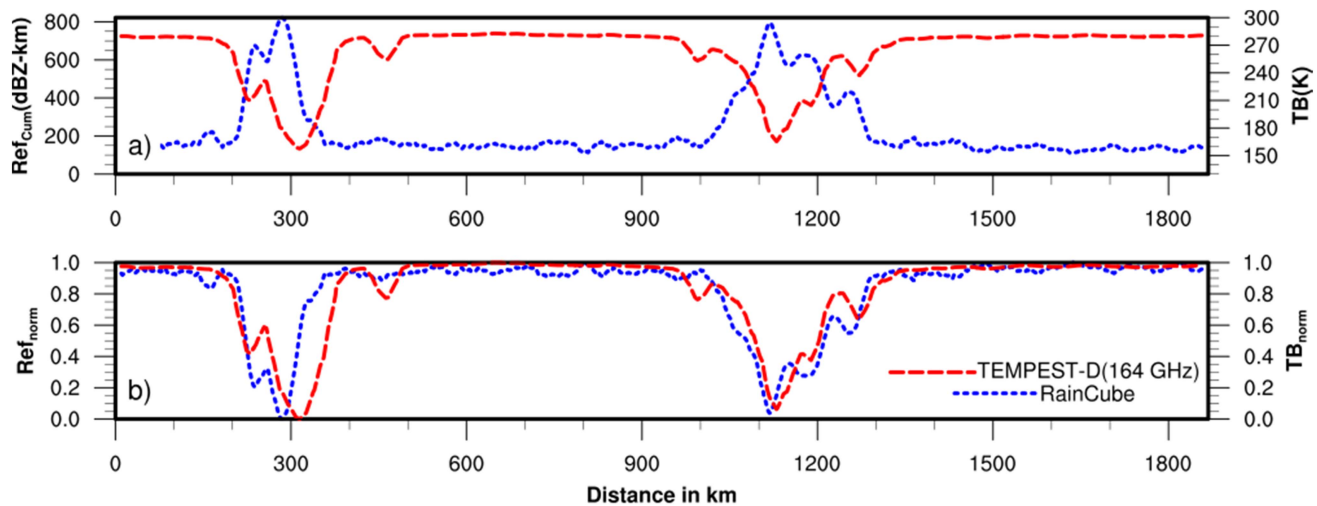


Fig. 6. Comparison of TEMPEST-D TBs at 164 GHz and RainCube cumulative reflectivity observations from a storm over Mexico's Pacific coast on October 15, 2018 (a) on original scale and (b) on a self-normalized scale with inverted RainCube observations.

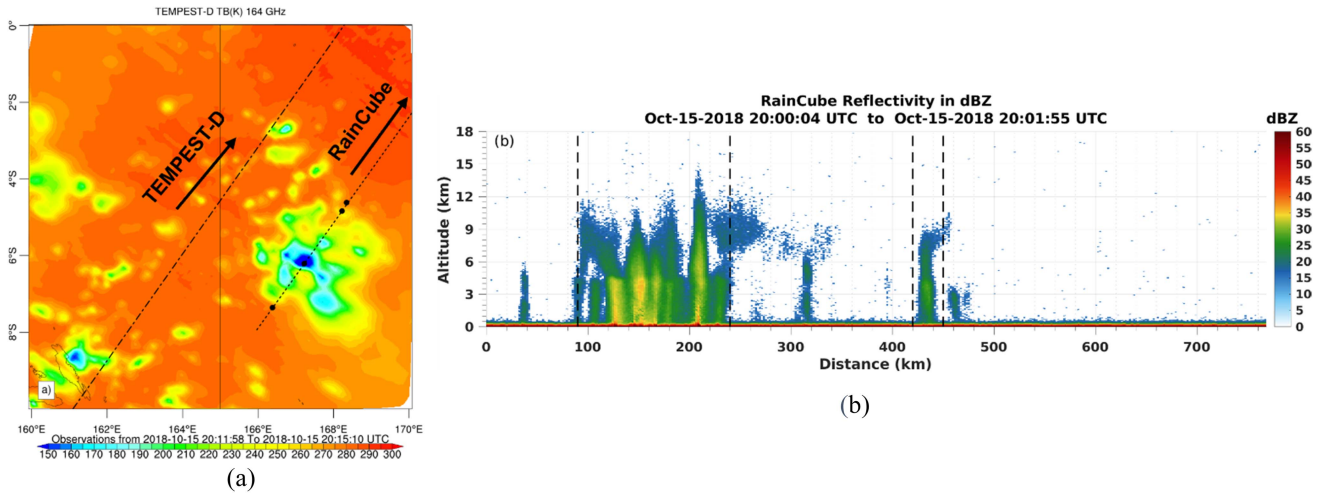


Fig. 7. (a) TEMPEST-D observed storm over the South Pacific Ocean near the Solomon Islands and the RainCube orbit paths on October 15, 2018. (b) RainCube vertical reflectivity profile observations from the same storm.

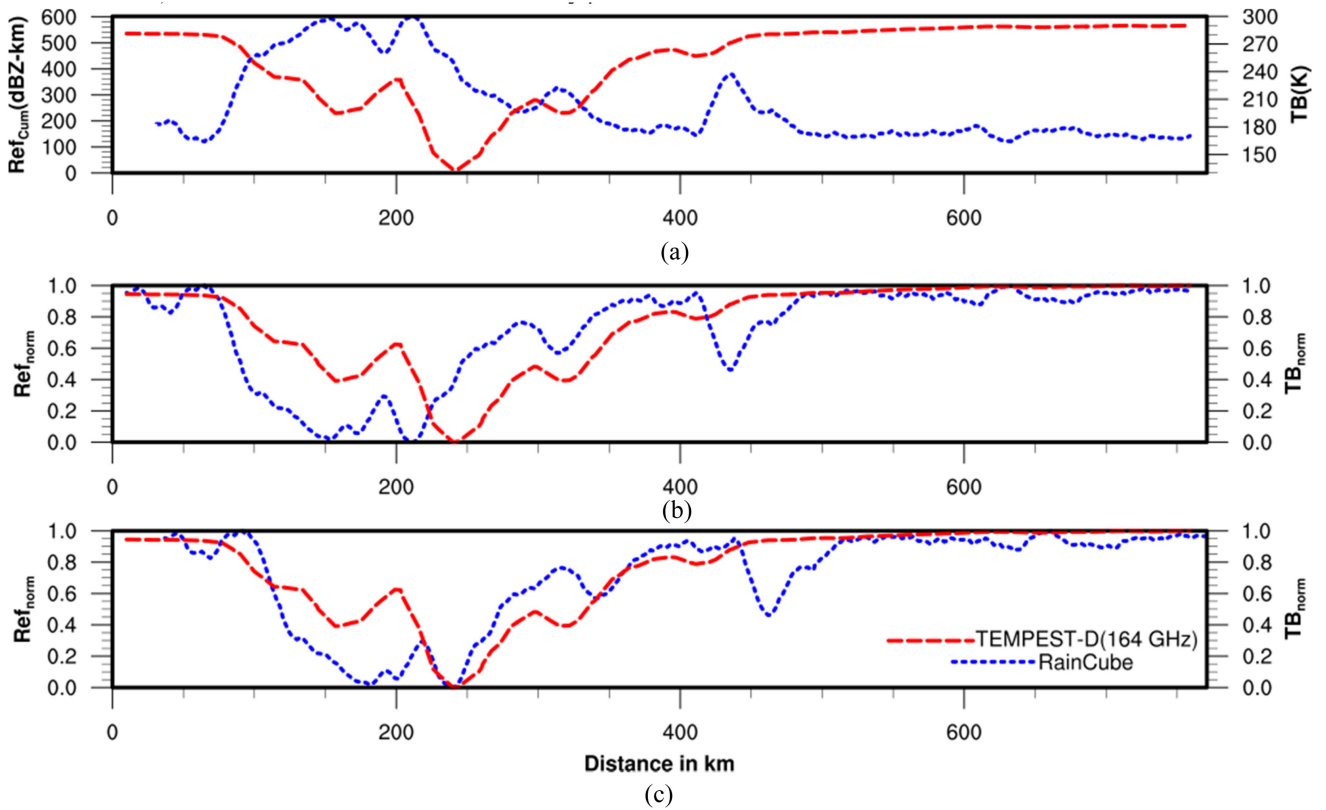


Fig. 8. TEMPEST-D and RainCube observations from a storm over the South Pacific Ocean near the Solomon Islands on October 15, 2018 (a) on original scale, (b) on self-normalized scale before shift correction, and (c) on self-normalized scale after shift correction. RainCube data are inverted in (b) and (c).

parallel paths in the same direction, from southwest to northeast. The TEMPEST-D TB image shows multiple intense storm cells and two cells along the path of RainCube. The black dots on the TEMPEST-D images in Fig. 5(a) correspond to the black vertical dotted lines in Fig. 5(b). The RainCube vertical reflectivity profile shows two peaks, corresponding to locations of two substantial decreases in the TEMPEST-D TBs. The RainCube

reflectivity indicates that both storm cells extended to 15 km above the surface. Fig. 5 shows that RainCube and TEMPEST-D observations agree well in terms of storm cell locations. Fig. 6 shows a comparison of range Ref_{Cum} observed by RainCube and 164 GHz TBs observed by TEMPEST-D. Fig. 6(a) shows the comparison on the original scale, and Fig. 6(b) shows the comparison on a self-normalized scale with inverted RainCube

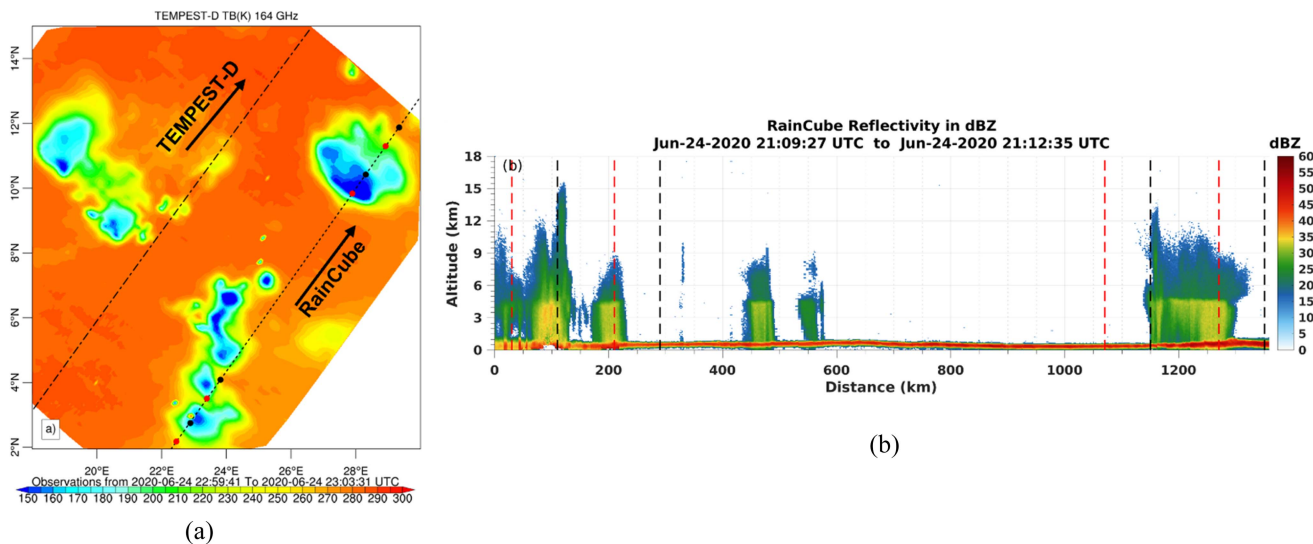


Fig. 9. (a) TEMPEST-D observed storm over the Central African Republic and the RainCube orbit paths on June 24, 2020. (b) RainCube vertical reflectivity profile observations from the same storm.

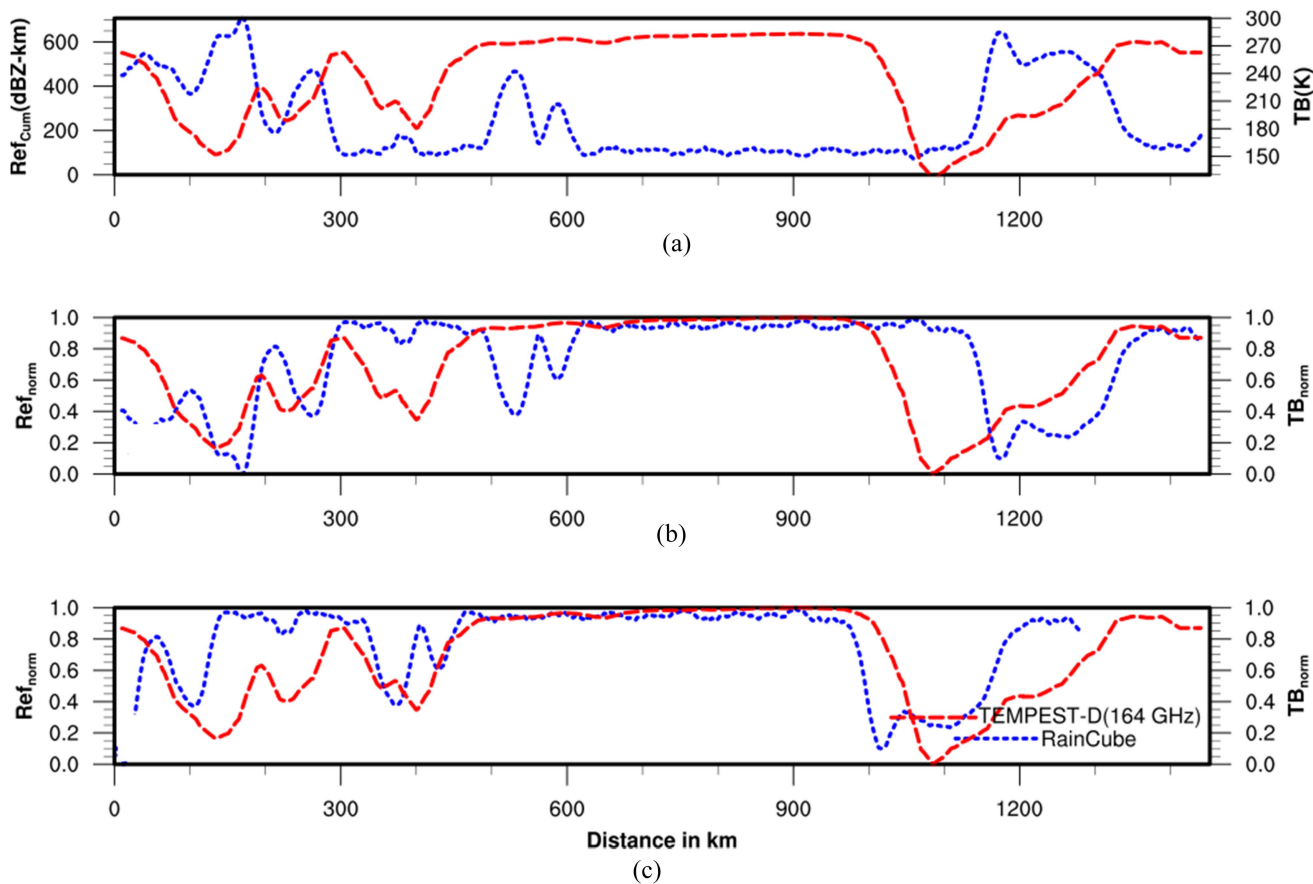


Fig. 10. Comparison of TEMPEST-D TBs at 164 GHz and RainCube cumulative reflectivity observations from a storm over the Central African Republic on June 24, 2020 (a) on original scale and (b) on a self-normalized scale before shift correction, and (c) on self-normalized scale after shift correction. RainCube data are inverted in (b) and (c).

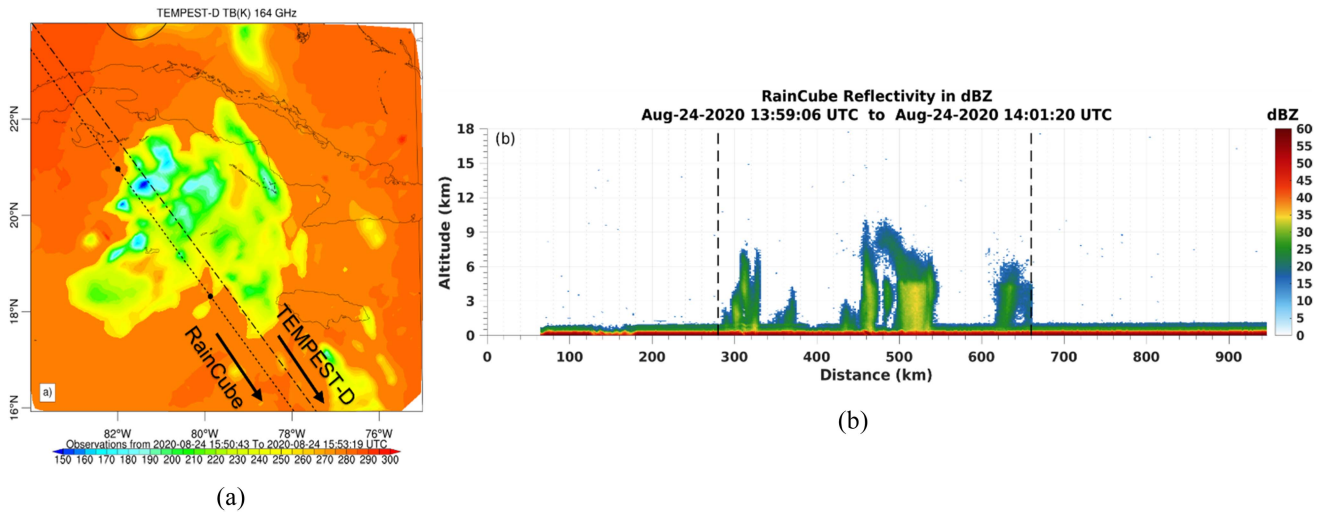


Fig. 11. (a) TEMPEST-D observations over Hurricane Laura on August 24, 2020 and the corresponding RainCube orbit paths. (b) RainCube vertical reflectivity profile observations from the same storm.

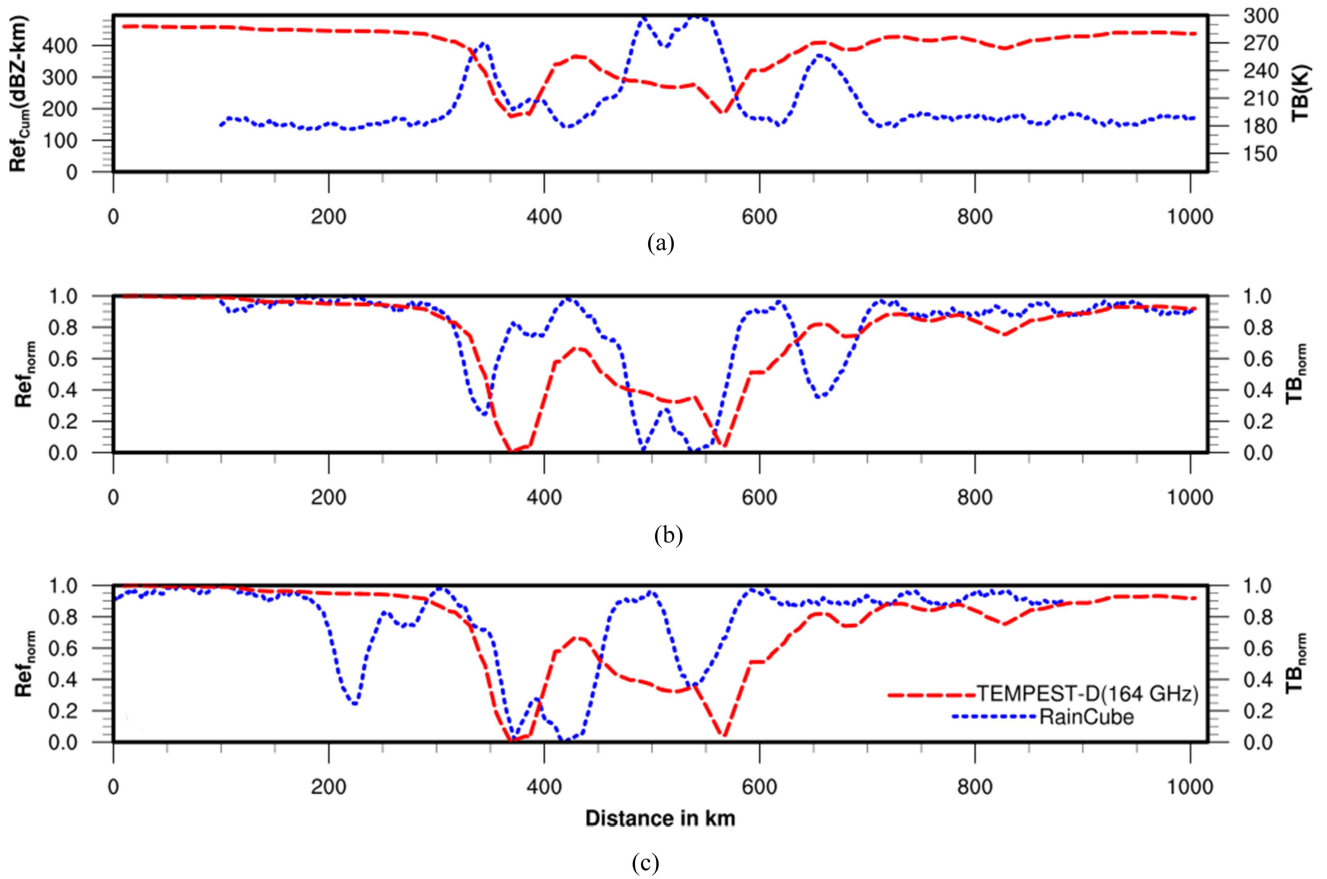


Fig. 12. TEMPEST-D and RainCube observations over Hurricane Laura on August 24, 2020 (a) on original scale, (b) on self-normalized scale before shift correction and (c) on self-normalized scale after shift correction. RainCube data are inverted in (b) and (c).

TABLE II
CORRELATION COEFFICIENTS BETWEEN SELF-NORMALIZED AND INVERTED RAINCUBE CUMULATIVE REFLECTIVITY AND SELF-NORMALIZED TEMPEST-D TBs BEFORE SPATIAL SHIFT CORRECTION

Channel (GHz) \ Event number	181	178	174	164	87
1	0.85	0.90	0.91	0.91	0.60
2	0.63	0.67	0.69	0.70	0.50
3	0.58	0.61	0.6	0.55	-0.23
4	0.46	0.73	0.80	0.80	-0.32
5	0.38	0.52	0.60	0.62	0.62
6	0.08	0.20	0.33	0.38	0.29
7	0.75	0.76	0.75	0.74	0.81
8	0.90	0.88	0.86	0.85	0.85
9	0.35	0.51	0.57	0.57	-0.01

TABLE III
CORRELATION COEFFICIENTS BETWEEN SELF-NORMALIZED AND INVERTED RAINCUBE CUMULATIVE REFLECTIVITY AND SELF-NORMALIZED TEMPEST-D TBs AFTER SPATIAL SHIFT CORRECTION

Channel (GHz) \ Event number	181	178	174	164	87
1	0.85	0.90	0.91	0.91	0.6
2	0.77	0.80	0.81	0.81	0.67
3	0.61	0.75	0.80	0.77	0.01
4	0.67	0.88	0.92	0.92	0.17
5	0.67	0.65	0.63	0.64	0.65
6	0.74	0.73	0.71	0.71	0.75
7	0.75	0.76	0.75	0.74	0.81
8	0.90	0.88	0.86	0.85	0.85
9	0.41	0.60	0.63	0.63	0.40

TABLE IV
CORRELATION COEFFICIENTS BETWEEN SELF-NORMALIZED AND INVERTED RAINCUBE CUMULATIVE REFLECTIVITY AND SELF-NORMALIZED TEMPEST-D TBs, AVERAGED OVER THE FOUR TEMPEST-D HIGH-FREQUENCY CHANNELS

Event number	Averaged correlation coefficient values			Time Difference (min)
	Before correction	After correction	Improvement (%)	
1	0.89	0.89	N/A	12
2	0.67	0.80	19	13
3	0.59	0.73	25	21
4	0.70	0.85	22	29
5	0.53	0.65	22	20
6	0.25	0.72	192	49
7	0.75	0.75	N/A	60
8	0.87	0.87	N/A	92
9	0.50	0.57	14	112
Average of all events	0.64	0.76	19	45

observations. The maximum value of Ref_{cum} for this storm is approximately 800 dBZ-km, and the lowest value of the 164 GHz TB is 160 K. The maximum values of Ref_{cum} and the minimum TB values are observed by both instruments at

nearly the same location. The RainCube observation clearly shows that the two storm cells produce rainfall at the surface. The reflectivity value varies from 30 to 35 dBZ at the inner cores of the storm cells, corresponding to moderate rainfall. The

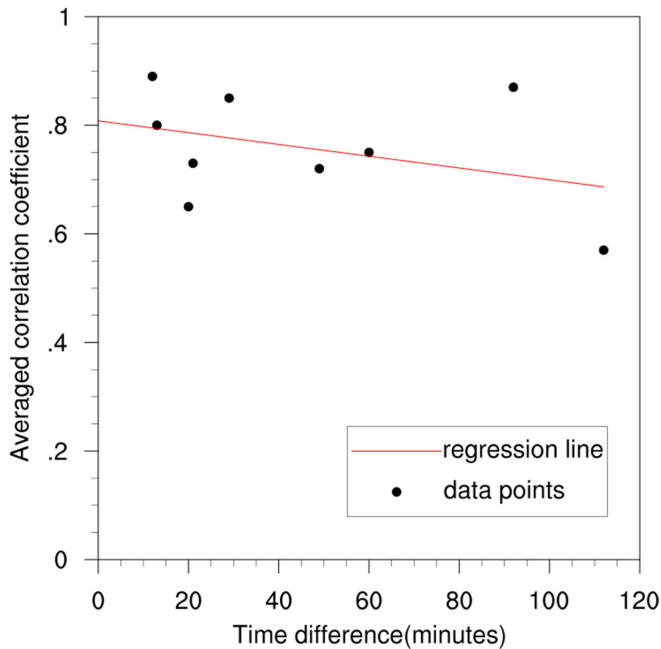


Fig. 13. Averaged correlation coefficient values for the four TEMPEST-D high-frequency channels with respect to the time difference between the TEMPEST-D and RainCube overpasses, along with the best-fit regression line.

RainCube radar observes precipitation due to backscattering from hydrometeors. A substantial scattering signature is also clearly observed in the TEMPEST-D TB observations. The TB values decrease from 280 to 160 K over the precipitating regions. Since both the TEMPEST-D and inverted RainCube time series decrease with increasing scattering, a correlation coefficient was calculated. Table II lists the correlation coefficients between self-normalized and inverted RainCube cumulative reflectivity ($Ref_{cum-norm}$) and self-normalized TEMPEST-D TB (TB_{norm}) for all five TEMPEST-D frequencies. In particular, the correlation coefficients for the 178, 174, and 164 GHz channels are at least 0.9, and the correlation coefficient for the 181 GHz channel is 0.85. In contrast, the 87 GHz channel has a low correlation coefficient of 0.6. The correlation coefficients are consistently higher for the four TEMPEST-D high-frequency channels than for the single low-frequency channel. This is expected since the low-frequency TEMPEST-D channel is mostly sensitive to the surface as well as integrated water vapor, which are not included in the radar at Ka -band signature. These qualitative and quantitative comparisons show that RainCube and TEMPEST-D data agree very well for this storm case, in terms of both location and intensity. Since the two measurements agree well, no shift correction was needed for this case.

B. Storm Over South Pacific Ocean

TEMPEST-D observations of a storm over the South Pacific Ocean near the Solomon Islands were performed on October 15, 2018 between 20:11 and 20:15 UTC, as shown in Fig. 7(a), along with the RainCube orbit path. Fig. 7(b) shows the RainCube observations over the storm on October 15, 2018 between

20:00 and 20:02 UTC. The time difference between these two observations was about 13 min. Both CubeSats were orbiting in the same direction, from southwest to northeast. The two black dots in Fig. 7(a) correspond to the locations of the vertical dotted lines in Fig. 7(b). It can be observed that the storm heights extend to 10–15 km altitude. Fig. 8(a) shows a comparison of RainCube Ref_{cum} and TEMPEST-D 164 GHz TB. The maximum value of Ref_{cum} for this case was approximately 600 dBZ-km at the center of the storm cell. The lowest TB value for this case was 130 K, 30 K smaller than for event 1. The large decreases in TB correspond to the high reflectivity at the center of the cell. It can be clearly seen in Fig. 7(b) that a narrow portion of the storm reached a reflectivity value of 40 dBZ. Fig. 8(b) and (c) shows the comparison of $Ref_{Cum-norm}$ and TB_{norm} before and after shift correction. Fig. 8(b) shows good match between the two observations with little shift. The shift correction algorithm is applied to the RainCube overpass data to match the TEMPEST-D overpass. The algorithm shifted the RainCube data by 28 km to the northeast to obtain a maximum correlation with TEMPEST-D observations. From event number 2 in Tables II and III, the correlation coefficients between self-normalized and inverted RainCube cumulative reflectivity ($Ref_{cum-norm}$) and self-normalized TEMPEST-D TB (TB_{norm}) have increased for all five TEMPEST-D frequencies after shift correction. For event number 2 in Table IV, the average correlation coefficient for the four TEMPEST-D high-frequency channels, i.e., 181, 178, 174, and 164 GHz, is 0.67. The shift correction algorithm increases the average correlation coefficient of the four high-frequency channels to 0.80, a 19% improvement. For the single low-frequency channel at 89 GHz, the correction algorithm improved the correlation coefficient from 0.5 to 0.67, a 34% improvement. Fig. 8(c) also shows good qualitative agreement between the self-normalized and inverted RainCube reflectivity and the self-normalized TB.

C. Storm Over Central African Republic

TEMPEST-D observations of a storm over the Central African Republic were performed on June 24, 2020 between 22:59 and 23:03 UTC, as shown in Fig. 9(a), along with the orbit path of RainCube. Fig. 9(b) shows the RainCube vertical reflectivity profiles for the storm on July 24, 2020 between 21:09 and 21:12 UTC. The time difference between these two observations was about 49 min. Both CubeSats were orbiting in the same direction, from southwest to northeast. The four black dots in Fig. 9(a) correspond to the four vertical dotted black lines in Fig. 9(b). The black dots and lines from Fig. 9(a) and (b) clearly show the shift in the time between the TEMPEST-D and RainCube observations. The correction algorithm corrected the shift of approximately 145 km by moving the RainCube observation in the southwest direction. The four red dots in Fig. 9(a) correspond to the four vertical dotted red lines in Fig. 9(b). The red dotted lines indicate the location of the storms from RainCube observations after the shift correction has been applied. The red dots and dotted lines in Fig. 9(a) and (b) clearly show that RainCube observed storm after shift correction matches the storm location observed by TEMPEST-D. The intensity pattern of the storm looks similar

in the two observations. Fig. 10(a) shows a comparison of RainCube Ref_{cum} and TEMPEST-D 164 GHz TB. For this case, the maximum value of Ref_{cum} was approximately 700 dBZ-km, and the lowest TB value was approximately 140 K. Fig. 10(b) and (c) shows the comparison of the self-normalized inverted RainCube observations with the self-normalized TEMPEST-D 164 GHz TB. Fig. 10(b) clearly shows the shift between the two observations, and Fig. 10(c) shows that the two storm locations match after the shift of approximately 145 km has been corrected by the correction algorithm. From event number 6 in Tables II and III, the correlation coefficients between self-normalized and inverted RainCube cumulative reflectivity ($\text{Ref}_{\text{cum-norm}}$) and self-normalized TEMPEST-D TB (TB_{norm}) have increased for all five TEMPEST-D frequencies after shift correction. For event number 6 in Table IV, the average correlation coefficient value over the four TEMPEST-D high-frequency channels is 0.25 before correction, and it increased to 0.72 after shift correction, an increase of 192%. For this case, the two observations, as shown in Fig. 9, agree well in terms of storm location and intensity.

D. Hurricane Laura

Hurricane Laura was a deadly and destructive Category 4 hurricane that made landfall in Cameron, Louisiana, on August 27, 2020. TEMPEST-D observations of Hurricane Laura over the Cayman Islands were performed on August 24, 2020, between 15:50 to 15:53 UTC, as shown in Fig. 11(a), along with the orbit path of RainCube. Fig. 11(b) shows the corresponding RainCube vertical reflectivity profile. Similar to previous cases, the two instruments were orbiting in the same direction except in a descending orbit, i.e., from northwest to southeast. The time difference between the two overpasses is 1 h and 52 min. The two black dots in Fig. 11(a) correspond to the two vertical dotted lines in Fig. 11(b). Fig. 12(a) shows a comparison of RainCube Ref_{cum} and TEMPEST-D 164 GHz TB. For this case, the maximum value of Ref_{cum} was approximately 500 dBZ-km, and the lowest TB value was approximately 190 K. Fig. 12(b) and (c) shows the comparison of the self-normalized inverted RainCube observations with the self-normalized TEMPEST-D 164 GHz TB. Fig. 12(b) clearly shows the shift between the two observations, and Fig. 12(c) shows that the two storm locations match after the shift of approximately 120 km has been corrected by the correction algorithm. From event number 9 in Tables II and III, the correlation coefficients between self-normalized and inverted RainCube cumulative reflectivity ($\text{Ref}_{\text{cum-norm}}$) and self-normalized TEMPEST-D TB (TB_{norm}) have increased for all five TEMPEST-D frequencies after shift correction. The comparison maps show that the pattern of the two observations looks similar. For event number 9 in Table IV, the average correlation coefficient value over the four TEMPEST-D high-frequency channels is 0.50 before correction, and it increased to 0.57 after shift correction, an increase of 14%. The average correlation coefficient value is lower than the previous cases due to the relatively long time between the RainCube and TEMPEST-D overpasses compared with the other cases. In addition to the storm motion between the two overpasses, Hurricane Laura also evolved between the RainCube and TEMPEST-D observations.

E. Regression Analysis

A regression model has been developed to determine the trend of the correlation coefficient with respect to the time difference between TEMPEST-D and RainCube observations. The averaged correlation coefficient values over the four TEMPEST-D high-frequency channels for all nine cases are used in the regression analysis. Table IV lists the averaged correlation coefficient value and the time difference between TEMPEST-D and RainCube observations for each of the nine cases. Fig. 13 shows the averaged correlation coefficient values for all nine cases as a function of the time difference between the two observations, along with the best-fit linear regression. The regression analysis clearly shows that the averaged correlation coefficient decreases as the time difference between TEMPEST-D and RainCube observations increases. When the regression line is extended to zero time difference, corresponding to a RainCube radar and a TEMPEST-D radiometer on the same small satellite, the averaged correlation coefficient is 0.81.

VI. CONCLUSION

Cross validation is performed between RainCube and TEMPEST-D microwave observations to study their physical consistency using nine storm cases scattered over many regions of the globe during a nearly two-year period. The results of this validation study demonstrate that RainCube and TEMPEST-D CubeSat observations are in very good qualitative and quantitative agreement. The correlation coefficient between the self-normalized and inverted RainCube cumulative reflectivity and the self-normalized TEMPEST-D TBs is greater for the four TEMPEST-D high-frequency channels near the water vapor absorption line at 183.31 GHz than for the low-frequency imaging channel near 90 GHz. This is expected since the low-frequency channel is mostly sensitive to the surface and integrated water vapor, which are not measured by the RainCube radar. A correction algorithm was developed to remove the uncertainty between RainCube and TEMPEST-D observations due to the time difference and the storm motion between the two sensors' overpasses. The correction algorithm improved the correlation coefficient averaged over all nine cases from 0.64 to 0.76 for the four TEMPEST-D high-frequency channels, a 19% increase on average. For the single TEMPEST-D low-frequency channel (87 GHz), the correction algorithm improved the correlation coefficient from 0.35 to 0.55, an increase of 58%. Regression analysis demonstrated that the averaged correlation coefficient decreases as the time difference between TEMPEST-D and RainCube increases. Extrapolation of the regression line to zero time difference leads to a correlation coefficient of 0.81 for a potential future deployment of a TEMPEST-D radiometer and a RainCube radar on the same small satellite.

ACKNOWLEDGMENT

The authors would like to thank T. Gaier, S. Brown, S. Padmanabhan, and B. Lim of JPL for producing the TEMPEST-D radiometer instrument and providing calibrated, geolocated brightness' temperatures, and P. Millar, G. Komar, B. Bauer,

and S. Babu for their on-going support, encouragement, and program management. TEMPEST-D is a collaborative program with Caltech/NASA Jet Propulsion Laboratory and Blue Canyon Technologies. A part of this research was performed at the Jet Propulsion Laboratory, under contract with the National Aeronautics and Space Administration.

REFERENCES

- [1] C. Radhakrishnan and V. Chandrasekar, "CASA prediction system over Dallas-Fort Worth urban network: Blending of nowcasting and high-resolution numerical weather prediction model," *J. Atmos. Ocean. Technol.*, vol. 37, no. 2, pp. 211–228, 2020.
- [2] J. Sun and N. A. Crook, "Dynamical and microphysical retrieval from Doppler radar observations using a cloud model and its adjoint—Part I: Model development and simulated data experiments," *J. Atmos. Sci.*, vol. 54, no. 12, pp. 1642–1661, 1997.
- [3] E. Gorgucci, V. Chandrasekar, V. N. Bringi, and G. Scarchilli, "Estimation of raindrop size distribution parameters from polarimetric radar measurements," *J. Atmos. Sci.*, vol. 59, no. 15, pp. 2373–2384, 2002.
- [4] V. N. Bringi, V. Chandrasekar, J. Hubbert, E. Gorgucci, W. L. Randeu, and M. Schoenhuber, "Raindrop size distribution in different climatic regimes from disdrometer and dual-polarized radar analysis," *J. Atmos. Sci.*, vol. 60, no. 2, pp. 354–365, 2003.
- [5] R. Chandrasekar and C. Balaji, "Impact of physics parameterization and 3DVAR data assimilation on prediction of tropical cyclones in the Bay of Bengal Region," *Natural Hazards*, vol. 80, no. 1, pp. 223–247, 2016.
- [6] D. Subramani, R. Chandrasekar, K. S. Ramanujam, and C. Balaji, "A new ensemble-based data assimilation algorithm to improve track prediction of tropical cyclones," *Natural Hazards*, vol. 71, no. 1, pp. 659–682, 2014.
- [7] R. Chandrasekar, R. K. Sahu, and C. Balaji, "Assimilation of multi-channel radiances in mesoscale models with an ensemble technique to improve track forecasts of tropical cyclones," *J. Earth Syst. Sci.*, vol. 131, no. 2, 2022, Art. no. 83.
- [8] R. Chandrasekar and C. Balaji, "Sensitivity of tropical cyclone Jal simulations to physics parameterizations," *J. Earth Syst. Sci.*, vol. 121, no. 4, pp. 923–946, 2012.
- [9] R. Mittal, M. Tewari, C. Radhakrishnan, R. Pallav, T. Singh, and A. K. Nickerson, "Response of Tropical Cyclone Phailin (2013) in the Bay of Bengal to climate perturbations," *Climate Dyn.*, vol. 53, pp. 2013–2022, 2019.
- [10] P. Mishra, S. R. Kannan, and C. Radhakrishnan, "The effect of anthropogenic heat and moisture on local weather at industrial heat islands: A numerical experiment," *Atmosphere*, vol. 13, 2022, Art. no. 357.
- [11] Y. V. Goncharenko, W. Berg, S. C. Reising, F. Iturbide-Sanchez, and V. Chandrasekar, "Design and analysis of CubeSat microwave radiometer constellations to observe temporal variability of the atmosphere," *IEEE J. Sel. Topics Appl. Earth Observ. Remote Sens.*, vol. 14, pp. 11728–11736, 2021, doi: [10.1109/JSTARS.2021.3128069](https://doi.org/10.1109/JSTARS.2021.3128069).
- [12] M. A. Swartwout, "CubeSat database," Accessed on: Apr. 14, 2022. [Online]. Available: <https://sites.google.com/a/slu.edu/swartwout/cubesat-database#h.2uocnm7j8arf>
- [13] W. Berg et al., "Calibration and validation of the TEMPEST-D CubeSat radiometer," *IEEE Trans. Geosci. Remote Sens.*, vol. 59, no. 6, pp. 4904–4914, Jun. 2021.
- [14] H. W. Christophersen et al., "Impact of TROPICS radiances on tropical cyclone prediction in an OSSE," *Monthly Weather Rev.*, vol. 149, no. 7, pp. 2279–2298, 2021.
- [15] C. Radhakrishnan, V. Chandrasekar, S. C. Reising, and W. Berg, "Cross validation of TEMPEST-D observations and GPM products over the precipitating systems," in *Proc. Fall Meeting Amer. Geophysical Union*, New Orleans, LA, USA, Dec. 13–17, 2021. [Online]. Available: <https://agu.confex.com/agu/fm21/meetingapp.cgi/Paper/1003709>
- [16] R. M. Schulte et al., "A passive microwave retrieval algorithm with minimal view-angle bias: Application to the TEMPEST-D CubeSat mission," *J. Atmos. Ocean. Technol.*, vol. 37, no. 2, pp. 197–210, 2020.
- [17] C. Radhakrishnan, V. Chandrasekar, W. Berg, and S. C. Reising, "Rainfall estimation from TEMPEST-D CubeSat observations: A machine-learning approach," *IEEE J. Sel. Topics Appl. Earth Observ. Remote Sens.*, vol. 15, pp. 3626–3636, 2022, doi: [10.1109/JSTARS.2022.3170835](https://doi.org/10.1109/JSTARS.2022.3170835).
- [18] S. C. Reising et al., "An earth venture in-space technology demonstration mission for temporal experiment for storms and tropical systems (TEMPEST)," in *Proc. IEEE Int. Geosci. Remote Sens. Symp.*, 2018, pp. 6301–6303.
- [19] S. Padmanabhan et al., "TEMPEST-D radiometer: Instrument description and prelaunch calibration," *IEEE Trans. Geosci. Remote Sens.*, vol. 59, no. 12, pp. 10213–10226, Dec. 2021.
- [20] E. Peral et al., "Radar technologies for earth remote sensing from CubeSat platforms," *Proc. IEEE*, vol. 106, no. 3, pp. 404–418, Mar. 2018.
- [21] O. O. Sy et al., "Scientific products from the first radar in a CubeSat (RainCube): Deconvolution, cross-validation, and retrievals," *IEEE Trans. Geosci. Remote Sens.*, vol. 60, 2022, Art. no. 1000320, doi: [10.1109/TGRS.2021.3073990](https://doi.org/10.1109/TGRS.2021.3073990).
- [22] C. Prabhakara, R. Iacovazzi, and J. M. Yoo, "TRMM precipitation radar and microwave imager observations of convective and stratiform rain over land and their theoretical implications," *J. Meteorol. Soc. Jpn. Ser. II*, vol. 80, no. 5, pp. 1183–1197, 2002.



Chandrasekar Radhakrishnan received the bachelor's degree from Anna University, Chennai, India, in 2006, and the Ph.D. degree from the Indian Institute of Technology Madras, Chennai, India, in 2013, both in mechanical engineering.

He was a Research Scientist with IBM India Research Laboratory, New Delhi, India. He is currently a Research Scientist with Cooperative Institute for Research in the Atmosphere, Colorado State University, Fort Collins, CO, USA. His research interests include numerical weather prediction, data assimila-

tion, satellite meteorology, radar-based nowcasting, and machine learning.



V. Chandrasekar (Fellow, IEEE) received the bachelor's degree from the Indian Institute of Technology Kharagpur, Kharagpur, India, in 1981, and the Ph.D. degree from Colorado State University (CSU), Fort Collins, CO, USA, in 1986, both in electrical engineering.

He was the Director of the Research Experiences for Undergraduate Program for more than 25 years, where he is involved in promoting research in the undergraduate curriculum. He is currently a University Distinguished Professor with CSU. He is also the Research Director of the National Science Foundation Engineering Research Center for Collaborative Adaptive Sensing of the Atmosphere. He has played a key role in developing the CSU-CHILL National Radar Facility as one of the most advanced meteorological radar systems available for research and continues to work actively with the CSU-CHILL radar, supporting its research and education mission. He is an avid experimentalist conducting special experiments to collect *in situ* observations to verify the new techniques and technologies. He has authored two textbooks and five general books and more than 250 peer-reviewed journal articles.

Dr. Chandrasekar was a recipient of numerous awards, including Knighted by the Government of Finland, the NASA Technical Contribution Award, NASA Group Achievement Award, the NASA Robert H. Goddard Exceptional Achievement Award, the Outstanding Advisor Award, IEEE GRSS Education Award, the National Oceanic and Atmospheric Administration (NOAA)/NWS Directors Medal of Excellence, and IEEE GRSS Distinguished Achievement Award. He is a Fellow of the American Meteorological Society, the American Geophysical Union, the International Union of Radio Science, NOAA, and Cooperative Institute for Research in the Atmosphere. He was the General Chair of IEEE International Geoscience and Remote Sensing Symposium (IGARSS 2006).



Steven C. Reising (Senior Member, IEEE) received the B.S.E.E. (*magna cum laude*) and M.S.E.E. degrees from Washington University, St. Louis, MO, USA, in 1989 and 1991, respectively, and the Ph.D. degree from Stanford University, Stanford, CA, USA, in 1998, all in electrical engineering.

He was an Assistant Professor of electrical and computer engineering with the University of Massachusetts Amherst, Amherst, MA, USA, where he received tenure. He served as a Summer Faculty Fellow for three summers with Remote Sensing Division,

Naval Research Laboratory, Washington, DC, USA. In 2004, he joined Colorado State University, Fort Collins, CO, USA, where he served as an Associate Professor, from August 2004 to June 2011, and has been a Full Professor of electrical and computer engineering since July 2011. He was a Principal Investigator of 19 grants from NASA, NOAA, the National Science Foundation (NSF), the Office of Naval Research, National Polar-Orbiting Operational Environmental Satellite System Integrated Program Office, European Space Agency, and Ball Aerospace and FIRST RF. He has served as a Principal Faculty Advisor for 16 M.S./Ph.D. students who have completed their degrees and are currently employed as professors, engineers, and researchers in universities, industry, and government laboratories. His research interests include a broad range of remote sensing disciplines, including microwave remote sensing of the Earth's atmosphere and oceans from airborne platforms, small satellites, and CubeSats; the design and development of radiometer systems from microwave to submillimeter-wave and THz frequencies (18–850 GHz); Lidar systems for sensing temperature and winds in the middle and upper atmosphere; and lightning-ionosphere interactions and atmospheric electrodynamic.

Dr. Reising was a recipient of the NSF CAREER Award in the areas of physical and mesoscale dynamic meteorology from 2003 to 2008, and the Office of Naval Research Young Investigator Program Award for passive microwave remote sensing of the oceans from 2000 to 2003. He is currently the Secretary of IEEE Geoscience and Remote Sensing Society (GRSS, 2021–present). He served as the Chair of the Ad-hoc Committee for Intersocietal Relations (2019–2020) and as an elected Administrative Committee (AdCom) Member of IEEE GRSS from 2003 to 2020 and IEEE Microwave Theory and Techniques Society (MTT-S) from 2014 to 2019. He served the IEEE as MTT-S Inter-Society Committee Chair from 2015 to 2018, GRSS Vice-President of Information Resources from 2011 to 2018, and the GRSS Vice-President of Technical Activities from 2008 to 2010. He was a Founding Member of *IEEE Geoscience and Remote Sensing Letters* Editorial Board and served as an Associate Editor from 2004 to 2013. He is a Guest Editor of three Special Issues and one Special Section of IEEE TRANSACTIONS ON GEOSCIENCE AND REMOTE SENSING. He served as the Immediate Past Chair of the U.S. National Committee of the International Union of Radio Science (USNC-URSI) from 2015 to 2017, the Chair from 2012 to 2014, and the Secretary from 2009 to 2011, of all ten URSI Commissions. He is a member of URSI Commissions F, G, and H, the American Meteorological Society, the American Geophysical Union, and the American Association for the Advancement of Science, Tau Beta Pi, and Eta Kappa Nu.



Wesley Berg received the B.S., M.S., and Ph.D. degrees in aerospace engineering from the University of Colorado, Boulder, CO, USA, in 1988, 1989, and 1993, respectively.

He worked with Cooperative Institute for Research in Environmental Science, NOAA's Environmental Research Laboratories, Boulder, CO, USA. He is a Senior Research Scientist with the Department of Atmospheric Science, Colorado State University, Fort Collins, CO, USA. His research interests include satellite remote sensing of precipitation and other hydrologic parameters with a focus on instrument calibration and the development

and analysis of satellite retrievals for long-term climate applications.



Shannon T. Brown (Senior Member, IEEE) received the B.S. degree in meteorology from Pennsylvania State University, State College, PA, USA, in 2001, and the M.S. degree in atmospheric science and the Ph.D. degree in geoscience and remote sensing from the University of Michigan, Ann Arbor, MI, USA, in 2003 and 2005, respectively.

He joined Microwave Advanced Systems Section, Jet Propulsion Laboratory (JPL), Pasadena, CA, USA, in 2005, as a member. He is a Principal Technologist with NASA JPL. He has been involved in the spaceborne Topex; Jason-1, 2, and 3 Microwave Radiometers; and the WindSat Polarimetric Radiometer. He is a Principal Investigator of the Compact Ocean Wind Vector Radiometer being developed for the U.S. Air Force and an Instrumental Scientist for the NASA Juno Microwave Radiometer on the Juno New Frontiers mission to Jupiter. He is a member of the Ocean Surface Topography Science Team, the Ocean Salinity Science Team, the SMAP Science Team, and the Juno Science Team. His research interests include microwave radiometer system development, calibration, geophysical algorithm development for both passive and active sensors, extraction of climate data records, and radiometer science.

Dr. Brown was a recipient of the NASA Exceptional Achievement Medal in 2009, the JPL Lew Allen Award in 2010, eight NASA group achievement awards, and the NASA Space Act Award in 2012.



Simone Tanelli received the Laurea degree in electrical engineering and the Ph.D. degree in remote sensing techniques from the University of Florence, Florence, Italy, in 1995 and 1999, respectively.

He is currently a Principal Engineer with Jet Propulsion Laboratory, California Institute of Technology, Pasadena, CA, USA. His main research interests include the design, operation, and data analysis of airborne and spaceborne cloud and precipitation radars.

Dr. Tanelli is a member of the NASA Precipitation Measurement Missions and CloudSat Science Teams, a Coleader for the Radar Studies Team within the NASA Aerosol, Clouds, and Ecosystem Mission Science Working Group, and the Leader for the CloudSat cloud-profiling-radar in-flight operations. He is a contributing member to the European Space Agency Earth Clouds, Aerosols, and Radiation Explorer mission via collaborative NASA/Japan Aerospace Exploration Agency/ESA activities.



Ousmane O. Sy received the Diplôme d'Ingénieur degree and PEGASUS certificate in aerospace engineering from École Nationale de Aviation Civile, Toulouse, France, in 2003, the M.Sc. degree in electrical engineering from the University of Toulouse III, Toulouse, France, in 2003, and the Ph.D. degree in electromagnetics from the Eindhoven University of Technology, Eindhoven, The Netherlands, in 2009.

In 2009, he joined Jet Propulsion Laboratory, where he has been working on atmospheric remote sensing instruments and mission concepts. His research interests include computational electromagnetics and stochastic uncertainty quantification.

search interests include computational electromagnetics and stochastic uncertainty quantification.

Gian Franco Sacco received the B.S. degree in theoretical nuclear physics from the University of Turin, Turin, Italy, in 1996, and the M.S. and Ph.D. degrees in theoretical particle physics from the University of Connecticut, Storrs, CT, USA, in 2000 and 2004, respectively.

He joined Jet Propulsion Laboratory as a Postdoctor in 2004 and became a staff Scientist in 2006. His research interests include algorithm development, numerical modeling, high-performance computing, and machine learning.